First Inertial Confinement Fusion Implosion Experiment in Octahedral Spherical Hohlraum

Ke Lan,[1,2,*] Yunsong Dong,[3] Junfeng Wu,[1,†] Zhichao Li,[3] Yaohua Chen,[1,‡] Hui Cao,[1] Liang Hao,[1] Shu Li,[1] Guoli Ren,[1] Wei Jiang,[3] Chuansheng Yin,[3] Chuankui Sun,[3] Zhongjing Chen,[3] Tianxuan Huang,[3] Xufei Xie,[3] Sanwei Li,[3] Wenyong Miao,[3] Xin Hu,[3] Qi Tang,[3] Zifeng Song,[3] Jiabin Chen,[3] Yunqing Xiao,[3] Xingsen Che,[3] Bo Deng,[3] Qiangqiang Wang,[3] Keli Deng,[3] Zhurong Cao,[3] Xiaoshi Peng,[3] Xiangming Liu,[3] Xiaoan He,[3] Ji Yan,[3] Yudong Pu,[3] Shaoyong Tu,[3] Yongteng Yuan,[3] Bo Yu,[3] Feng Wang,[3] Jiamin Yang,[3] Shaoen Jiang,[3] Lin Gao,[3] Jun Xie,[3] Wei Zhang,[3] Yiyang Liu,[3] Zhanwen Zhang,[3] Haijun Zhang,[3] Zhibing He,[3] Kai Du,[3] Liquan Wang,[3] Xu Chen,[3] Wei Zhou,[3] Xiaoxia Huang,[3] Huaiwen Guo,[3] Kuixing Zheng,[3] Qihua Zhu,[3] Wanguo Zheng,[3] Wen Yi Huo,[1] Xudeng Hang,[1] Kai Li,[1] Chuanlei Zhai,[1] Hui Xie,[1] Lingxiao Li,[1] Jie Liu,[2,4] Yongkun Ding,[1,2] and Weiyan Zhang[5,2]

[1]*Institute of Applied Physics and Computational Mathematics, Beijing 100094, China*
[2]*HEDPS, Center for Applied Physics and Technology, and College of Engineering, Peking University, Beijing 100871, China*
[3]*Research Center of Laser Fusion, China Academy of Engineering Physics, Mianyang 621900, China*
[4]*Graduate School, China Academy of Engineering Physics, Beijing 100193, China*
[5]*China Academy of Engineering Physics, Mianyang 621900, China*

(Received 3 September 2021; revised 1 November 2021; accepted 19 November 2021; published 10 December 2021; corrected 3 March 2022)

In inertial confinement approaches to fusion, the asymmetry of target implosion is a major obstacle to achieving high gain in the laboratory. A recently proposed octahedral spherical hohlraum makes it possible to naturally create spherical target irradiation without supplementary symmetry control. Before any decision is made to pursue an ignition-scale laser system based on the octahedral hohlraum, one needs to test the concept with the existing facilities. Here, we report a proof-of-concept experiment for the novel octahedral hohlraum geometry on the cylindrically configured SGIII laser facility without a symmetry control. All polar and equatorial self-emission images of the compressed target show a near round shape of convergence ratio 15 under both square and shaped laser pulses. The observed implosion performances agree well with the ideal spherical implosion simulation. It also shows limitations with using the existing facilities and adds further weight to the need to move to a spherical port geometry for future ignition laser facilities.

DOI: 10.1103/PhysRevLett.127.245001

Laser indirect-drive inertial confinement fusion (ICF) is one of the main approaches for achieving ignition of nuclear fusion reactions in the laboratory [1]. A highly symmetric irradiation is a prerequisite for compressing the spherical deuterium-tritium fuel capsule to the extreme conditions similar to those at the center of the Sun [2,3]. To create a temporal spherical radiation drive inside a cylindrical hohlraum, elaborate tuning technologies [4–8] have been developed at the National Ignition Facility (NIF) [9–12] since its completion in 2009. Important milestones [13–15] have been achieved on the quest for ignition at the NIF. The superexciting one is that the NIF has taken a major leap toward the ignition goal with a remarkable 1.3 MJ output triggered by 1.9 MJ laser energy [16]. This is the clue to make progress toward simple and robust target designs at an upgrade facility for achieving repeatable and predictable high gains and studying ignited targets in detail. Major obstacles preventing high gain fusion still remain [17–19], including asymmetry of target irradiation [4,5,7], laser plasma instabilities (LPIs) [20–22], and hydrodynamic instabilities [23–25], which are strongly connected with the hohlraum configuration and laser arrangement.

Though all present laser facilities for the indirect-drive approach are configured for the hohlraums with a cylindrical symmetry [1,26–34], various hohlraum configurations have been proposed and investigated [35,36]. In Ref. [37], the authors used the 60-beam OMEGA laser to test the concept of the tetrahedral hohlraum with four equivalent laser entrance holes (LEHs), achieving a convergence ratio of ~10 under radiation drive temperatures of 180 to 229 eV without symmetry tuning. However, the dominating spherical harmonics of the tetrahedral hohlraum is Y_{32}, whose asymmetry smoothing factor remains higher than about 14% even at a hohlraum-to-capsule radius ratio of 5 [1,3,38]. Here, Y_{lm} is the spherical harmonic of the polar mode l (viewed from the equator) and the azimuthal mode m (viewed from the pole) defined in quantum mechanics. Thus, the technology of dynamical compensation by using two sets of laser beams was proposed [35] to decrease the asymmetry inside a

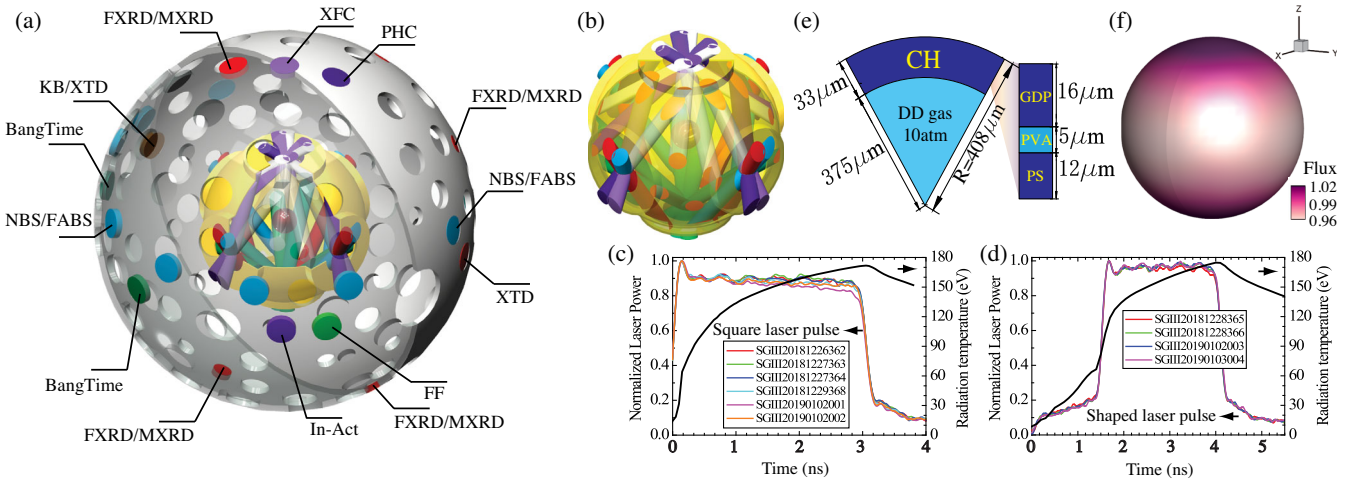

FIG. 1. (a) Schematic diagrams of the experimental setup with diagnostics and the 32-beam optimum repointing scheme. The gray sphere represents the target chamber with major diagnostic ports; the golden sphere represents the six-hole hohlraum with laser beams entering through two polar and four equatorial ports; the wine sphere at the center represents the capsule. (b) Scenography of the laser beam configuration and the laser spots on the hohlraum wall. (c) Square laser pulses (colored lines) for different shots and $T_{r,\mathrm{cap}}$ (black line) for shot SGIII20181227364, which is the temporal space-averaged x-ray radiation drive on the capsule from postshot simulations with LARED-INTEGRATION. (d) Shaped laser pulses (colored lines) for different shots and $T_{r,\mathrm{cap}}$ (black line) for shot SGIII20190102003. (e) Layered capsule diagram. (f) Scenography of the radiation flux distribution on the capsule ablation surface at 1.5 ns for shot SGIII20190102003.

tetrahedral hohlraum, which nevertheless brings challenges to theory, simulation, and technology.

A recently proposed octahedral spherical hohlraum [38–40] (hereafter simplified as octahedral hohlraum) has the advantage of robustly generating a full-time highly symmetric radiation drive without symmetry tuning, such as wavelength detuning on lasers beams and beam depointing. The octahedral hohlraum has six LEHs. In an ideal configuration [38], all laser beams enter the LEHs at an identical angle θ_L in a range of 50° to 60°. Such irradiation scheme has the advantages of no beam crossing inside the hohlraum, no laser spot overlapping, and no disturbance between the laser beam propagation and ablated material from the capsule. Distribution of x-ray radiation in an octahedral hohlraum does not contain asymmetries corresponding to the spherical harmonic modes $l = 2$ and all odd l, and asymmetry of $l = 6$ is at a very low level. Choosing a hohlraum-to-capsule radius ratio of about 5, named the golden radius ratio in Ref. [39], the mode $l = 4$ is also suppressed, thus leaving $l = 8$ as the dominating mode. This novel approach is unique and has initiated a broad interest in the ICF community [41–44]. Note that the ideal laser configuration of octahedral geometry can be applied to other approaches [45,46].

Experimental campaigns on octahedral hohlraum began to be carried out in 2014 on the SGIII [47], addressing various important aspects of this novel hohlraum configuration [48–53]. However, an implosion experiment with an octahedral hohlraum has not been done previously. To create high symmetry radiation on a capsule, very different from Ref. [52], it requires all LEHs to be of the same size and a beam pointing to approach the ideal beam configuration of the octahedral hohlraum as close as possible. The LEH size is determined by beam injection angles, beam focal spots at the LEH, beam pointing error, and LEH closures under radiation. At the SGIII, all beams have a 0.25-mm-radius round focal spot at the polar LEHs. Their focal spots at the equatorial LEHs are elliptical with a major radius of about 0.47 mm if injected at ~60°. Considering the LEH closure under 175 eV and a laser pointing error of 0.07 mm, we use 0.7-mm-radius LEHs for the 2.4-mm-radius SGIII scale the octahedral hohlraum in this implosion experiment. The cylindrical LEHs are used with a 1.2-mm-radius outer ring.

Shown in Fig. 1(a) is the experimental setup with diagnostics and the 32-beam optimum repointing scheme obtained after investigating tens of possibilities of the SGIII. As shown, there are four beams entering each equatorial LEH with two beams entering at θ_L of 61.5° and two beams at 62.1°, and there are eight beams entering each polar LEH with four beams at an angle of 49.5° and four beams at 55°. All injection angles are sufficiently close to the ideal configuration of 50° to 60°. The laser spot pattern on the hohlraum wall is shown in Fig. 1(b). The polar beams send energy to the equator, while the equatorial beams send energy to the poles, explaining why there are twice as many beams through each polar LEH. In our design, we use a two-dimensional (2D) multigroup radiation hydrodynamic code LARED-INTEGRATION with a two-different-size LEH model to simulate the hohlraum energetics, a 2D capsule-only multigroup radiation hydrodynamic code LARED-S to simulate the implosion dynamics

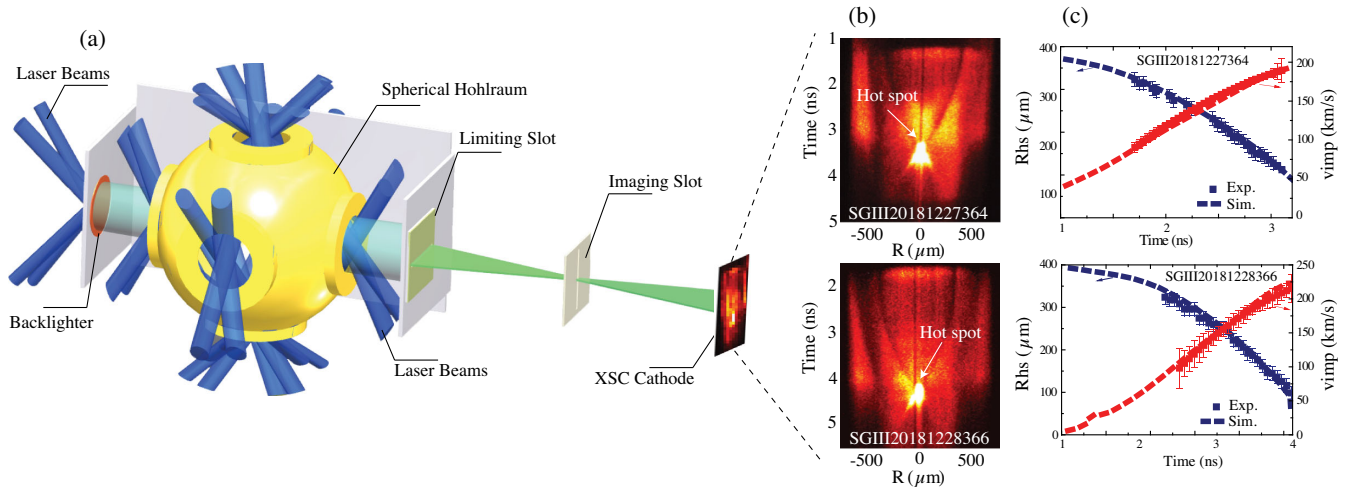

FIG. 2. (a) Target configuration with side-target radiography to measure the implosion trajectory of the capsule via an XSC. (b) Implosion trajectory recorded by an XSC for SGIII20181227364 under the square pulse (upper) and for SGIII20181228366 under the shaped pulse (lower). (c) Comparisons of the observed implosion trajectory $R(t)$ (blue squares) and velocity $v(t) = dR(t)/dt$ (red squares) with the postshot 1D simulations (blue and red dashed lines) from a capsule-only multigroup radiation hydrodynamic code LARED-S.

and hydrodynamic instabilities, a 3D view factor code VF3D to calculate the radiation asymmetry on the capsule, and a postprocessor HLIP to investigate the LPI. Details of the optimum repointing scheme, simulation codes [39,54–60], models and methods used in simulation [61–68], and diagnostics [32,69–71] are presented in Ref. [72].

The octahedral hohlraum is filled with a gas neopentane (C_5H_{12}) of initial density 1.3 mg/cc with windows covered by 0.5 μm polyamide films. As shown in Figs. 1(c) and 1(d), we use the 3 ns square and 4 ns shaped laser pulses to generate the single-step and two-step x-ray pulses, respectively. The maximum radiation temperature in the hohlraum is about 175 eV under 85 kJ. Here, it is instructive to compare with Ref. [37], where the authors obtained a radiative temperature of 180 eV with a much lower drive energy of 22 kJ and 2 ns duration at the OMEGA. The difference is mostly due to the hohlraum size. Reference [37] used a much smaller hohlraum of 1.4 mm radius, while here, with the 0.7-mm-radius LEHs, we need a 2.4-mm-radius hohlraum to maintain a high symmetry on the capsule. As a result, it has a much lower temperature in our experiment.

The plastic capsule in Fig. 1(e) contains D_2 gas of initial density 1.8 mg/cm^3. Shown in Fig. 1(f) is the radiation flux distribution on the capsule ablation surface calculated by VF3D by taking the ablation surface at 0.5 mm and a spot-to-wall flux ratio as 2:1 valid at 1.5 ns for shot SGIII20190102003 [72]. As shown, the polar flux is higher than the equatorial. This is caused by the optimum repointing scheme [Fig. 1(b)], which contains residual imbalances between the polar and equatorial beams and leads to, very different from the case of ideal octahedral hohlraums, a mode $l = 2$ asymmetry. In this proof-of-concept experiment, we take the hohlraum-to-capsule radius ratio as 5.9 to balance the trade-offs among the needs for a high neutron yield and a high convergence ratio under the 175 eV radiation. From LARED-S, both x-ray pulses drive the capsule to a convergence ratio of about 15 but with different implosion dynamics [72]. The two-step pulse implodes the capsule to a higher velocity, leading to a higher ion temperature T_i and further producing a neutron yield of 25% higher than the single-step pulse.

The implosion dynamics was measured with the soft x-ray radiography diagnostic shown in Fig. 2(a). A backlighter Pb plate was illuminated by four beams of SGIII, and the transmitted radiation was recorded with the x-ray streak camera (XSC) through the two LEHs and imaging slots. Notice that the octahedral hohlraum has the advantage over the cylindrical hohlraum of having the possibility of using opposite equatorial LEHs for radiography diagnostics. Shown in Fig. 2(b) are the implosion trajectories recorded by the XSC for shots SGIII20181227364 driven by the square pulse of 79.5 kJ and SGIII20181228366 by the shaped pulse of 78.5 kJ. In all postshot simulations, we use the measured parameters of the target and laser for each shot. The implosion trajectories and velocities are compared to the postshot 1D simulations from LARED-S in Fig. 2(c), showing very good agreement with the measurements. It reveals a high implosion symmetry achieved in the experiment.

From LARED-S, the growth factors of the perturbations seeded on the CH surface reach their peak of only 40 for mode $l = 30$ on the ablation front and peak of 30 for $l = 20$ at the CH/D_2 interface [72], which is reasonable for such an implosion with a convergence ratio of 15 under 175 eV radiation. Thus, the implosion is hydrodynamically stable and compromised only by low mode asymmetries. Hereafter, we focus on the perturbations corresponding

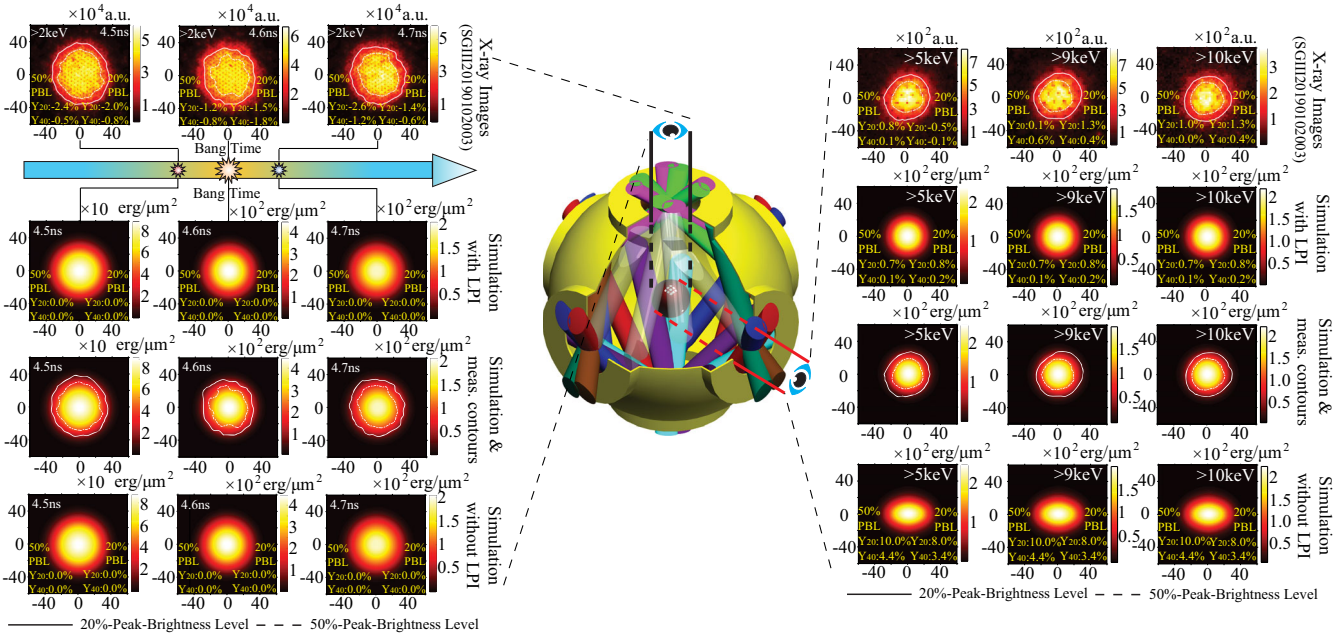

FIG. 3. Comparisons of polar (left) and equatorial (right) self-emission images between the experiment and postshot 2D simulation for SGIII20190102003. First row shows time-resolved polar self-emission images from an x-ray framing camera at 4.5, 4.6, and 4.7 ns (left, with system resolution of ~17 μm and pixel value of 0.9 μm at the object space) and time-integrated equatorial self-emission images from a pinhole camera with different filters for x-ray emissions above 5, 9, and 10 keV (right, with system resolution of ~19 μm and pixel value of 2.5 μm at the object space). The red spots in the center hottest regions are due to the space resolution. The solid and dotted lines are contours of 20% and 50% peak emissions, respectively, with their contour asymmetries Y_{20} and Y_{40} at the image bottom. Here, Y_{8m} is too small to be analyzed with our present technology. The second row shows polar (left) and equatorial (right) images from postshot 2D simulation with LPI taken into account in the asymmetry calculation. The third row shows superimpositions of the measured contour lines on the simulation images. The fourth row shows polar (left) and equatorial (right) images from postshot 2D simulation without accounting for LPI in the asymmetry calculation.

to the modes $l = 2$ and $l = 4$. From VF3D, Y_{6m} and Y_{8m} can be neglected because their amplitudes are much lower than Y_{2m} and Y_{4m} for this experiment. Further notice that Y_{44} is a fully 3D mode, with completely different polar and azimuthal angle ranges from Y_{40}. Thus, we only consider Y_{20} and Y_{40} for the asymmetry study.

Asymmetry of an octahedral hohlraum is mainly decided by two radius ratios and two flux ratios, which are R_H/R_C^*, R_{LEH}^*/R_C^*, F_S/F_W, and F_{LEH}/F_W [72]. Here, R_H is the hohlraum radius, R_C^* is the position where asymmetries are applied to the radiation flux on the capsule, and R_{LEH}^* is the LEH radius with closure behavior; F_W, F_S, and F_{LEH} are fluxes from the hohlraum wall, laser spot, and closing LEH, respectively. The temporal behaviors of these ratios can be obtained from 2D simulations. From measurement, the averaged backscattered fraction of equatorial beams is remarkably higher than that of the polar [72]. Aroused by imbalances between polar and equatorial beams, Y_{20} is seriously influenced by F_S/F_W, which is strongly connected with the flux or energy difference among the beams. In VF3D, we consider the measured input laser energy and laser backscatters as multipliers on F_S/F_W separately for each beam. Temporal scattered percentages are obtained from the measured backscattered spectra. Note that imbalances between the polar and equatorial beams not only directly lead to Y_{20} but also possibly indirectly lead to an asymmetry due to different LEH closing rates. However, our 2D simulations show there is little difference between the LEH closure behaviors and the polar and equatorial LEHs, so we take the same polar and equatorial LEH closure behaviors in VF3D. As compared to the case without LPI in the asymmetry calculations, Y_{20} is significantly suppressed by the strong laser backscatters of equatorial beams during the flattop of the second step laser [72]. In contrast, Y_{40} is much simpler, which is mainly decided by R_H/R_C^* at $R_H/R_C^* \sim 5$. According to our design, R_H/R_C^* is around 5, so Y_{40} is close to zero during the whole shock transition phase. In the acceleration phase, the smoothing factor of Y_{4m} is very small with little change at $R_H/R_C^* > 7$, so Y_{40} slowly increases as time and keeps lower than 0.5%. Thus, it results in a quasispherical symmetry with the compensation of LPI.

In Fig. 3, we compare the measured polar and equatorial self-emission images of the hot spot with the postshot 2D simulation for SGIII20190102003 driven by the shaped laser pulse. The x-ray framing camera from the polar view records the time-resolved images of the hot spot via x-ray emissions above 2 keV, and a pinhole camera records the time-integrated images in the equatorial plane with different filters. As shown, both polar and equatorial

self-emission images are quasispherical. For equatorial images, the contours with different filters have almost the same size, indicating that all these x-rays are mainly generated from the same region where fusion reactions take place. The postshot 2D simulations with LPI taken into account well reproduce the experimental images. As a comparison, without LPI, the simulation generates a pancake image from the equatorial view due to a beam imbalance of the repointing scheme as in Fig. 1(b).

Our experimental results are repeatable. For all effective shots with neutron yield measurement, the neutron yield ratio of the scintillation detector to the 1D simulation is above 55% under both square and shaped laser pulses. A summary of the key measurements and postshot simulated implosion performances is given in Ref. [72] for SGIII20181227364 and SGIII20190102003, which have different pulse shapes but similar laser energies. The neutron yield ratio of the scintillation detector to the 1D simulation is 84% and to the 2D simulation is 89% for SGIII20181227364, and 71% and 73% for SGIII20190102003, respectively. Similar to the NIF shots N130927 [13], N130812 [73], N191007, and N191110 [15], both SGIII20181227364 and SGIII20190102003 have lower measured neutron yields while higher ion temperatures than simulations. The reason should be investigated in the future work.

We have implemented a proof-of-concept experiment for the octahedral hohlraum geometry on the SGIII without symmetry control. The 1D implosion simulations agree very well with the measurements, revealing a very high symmetry possibly achieved in the experiment. Note that it is more of a LPI-compensated test than a straight test of the optimized octahedral scheme, which in turn indicates limitations with the existing laser facilities for octahedral hohlraum studies. The beam imbalance of the repointing scheme can lead to the sensitivity of Y_{2m} to power balance and difference in LEH closure rates, which further increases the complexity of asymmetry mitigation. However, the history of the field shows that lessons learned on one facility help in the design of the next, and our results add further weight to the need to move to an octahedral geometry for ignition-scale laser systems.

The authors would like to thank the entire SGIII operations, diagnostics, and target teams at the Research Center of Laser Fusion, Chinese Academy of Engineering Physics for their outstanding support during the experiment. All simulations were performed on the supercomputer in China. K. L. especially appreciates Professor Vladimir Tikhonchuk of the ELI-Beamlines for beneficial discussions. This work is supported by the National Natural Science Foundation of China (Grants No. 12035002 and No. 11775033).

K. L. and Y. D. contributed equally to this work. K. L. was the lead scientist for the octahedral spherical hohlraum campaign, the implosion experiment with octahedral spherical hohlraum, the target and laser strategies, and wrote the paper. Y. D. was the lead experimentalist on the first implosion experiment with the octahedral spherical hohlraum. J. W. was the lead scientist for the capsule design, performed the 1D design, 2D models of stability and asymmetry, and the pre- and postshot analysis of implosion performances. Z. L. was the lead experimentalist on the hohlraum energetics diagnostic design. Y. C. performed all 2D simulations of pre- and postshot studies of the hohlraum energetics and created all figures. H. C. performed the study of the repointing scheme for the octahedral spherical hohlraum and performed all pre- and postshot analyses of radiation asymmetries with VF3D. L. H. performed all pre- and postshot analyses of laser-plasma instabilities with HLIP. S. L. performed the three-dimensional simulations of hohlraum energetics with IMC3D. G. R. performed the comparisons of 1D implosion performances with RDMG and LARED-S. W. J., C. Y., C. S., Z. C., T. H., X. X., S. L., W. M., X. H., Q. T., Z. S., J. C., Y. X., X. C., B. D., Q. W., K. D., Z. C., X. P., X. L., X. H. J. Y., Y. P., S. T., Y. Y., B. Y., F. W., J. Y., and S. J. were responsible for the diagnostics, building the experiment platform, and processing the data. L. G., J. X., W. Z., Y. L., Z. Z., H. Z., Z. H., and K. D. were responsible for target fabrication. L. W., X. C., W. Z., X. H., H. G., K. Z., Q. Z., and W. Z. were responsible for laser operation. W. Y. H., X. H., K. L., C. Z., H. X., L. L., J. L., Y. D., and W. Z. took part in discussions on the experiment.

*lan_ke@iapcm.ac.cn
†wu_junfeng@iapcm.ac.cn
‡chen_yaohua@iapcm.ac.cn

[1] J. Lindl, Development of the indirect-drive approach to inertial confinement fusion and the target physics basis for ignition and gain, Phys. Plasmas **2**, 3933 (1995).
[2] E. M. Campbell, and W. J. Hogan, The National Ignition Facility—applications for inertial fusion energy and high-energy-density science, Plasma Phys. Controlled Fusion **41**, B39 (1999).
[3] S. Atzeni and J. Meyer-ter-Vehn, *The Physics of Inertial Fusion* (Oxford University Press, New York, 2004).
[4] P. Michel *et al.*, Tuning the Implosion Symmetry of ICF Targets via Controlled Crossed-Beam Energy Transfer, Phys. Rev. Lett. **102**, 025004 (2009).
[5] J. D. Moody *et al.*, Multistep redirection by cross-beam power transfer of ultrahigh-power lasers in a plasma, Nat. Phys. **8**, 344 (2012).
[6] D. A. Callahan, O. A. Hurricane, J. E. Ralph *et al.*, Exploring the limits of case-to-capsule ratio, pulse length, and picket energy for symmtric hohlraum drive on the National Ignition Facility Laser, Phys. Plasmas **25**, 056305 (2018).
[7] A. L. Kritcher *et al.*, Symmetric fielding of the largest diamond capsule implosions on the NIF, Phys. Plasmas **27**, 052710 (2020).

[8] A. L. Kritcher, A. B. Zylstra, D. A. Callahan *et al.*, Achieving record hot spot energies with large HDC implosions on NIF in HYBRID-E, Phys. Plasmas **28**, 072706 (2021).
[9] E. I. Moses, R. N. Boyd, B. A. Remington, C. J. Keane, and R. Al-Ayat, The National Ignition Facility: Ushering in a new age for high energy density science, Phys. Plasmas **16**, 041006 (2009).
[10] S. W. Haan, J. D. Lindl, D. A. Callahan, D. S. Clark, J. D. Salmonson, B. A. Hammel *et al.*, Point design targets, specifications, and requirements for the 2010 ignition campaign on the National Ignition Facility, Phys. Plasmas **18**, 051001 (2011).
[11] A. N. Simakov, D. C. Wilson, S. A. Yi, J. L. Kline, D. S. Clark, J. L. Milovich, J. D. Salmonson, and S. H. Batha, Optimized beryllium target design for indirectly driven inertial confinement fusion experiments on the National Ignition Facility, Phys. Plasmas **21**, 022701 (2014).
[12] J. Nilsen, A. L. Kritcher, M. E. Martin, R. E. Tipton, H. D. Whitley, D. C. Swift *et al.*, Understanding the effects of radiative preheat and self-emission from shock heating on equation of state measurement at 100s of Mbar using spherically converging shock waves in a NIF hohlraum, Matter Radiat. Extremes **5**, 018401 (2020).
[13] O. A. Hurricane, D. A. Callahan, D. T. Casey, P. M. Celliers, C. Cerjan, E. L. Dewald *et al.*, Fuel gain exceeding unity in an inertially confined fusion implosion, Nature (London) **506**, 343 (2014).
[14] S. Le Pape, L. F. BerzakHopkins, L. Divol, A. Pak, E. L. Dewald, S. Bhandarkar *et al.*, Fusion Energy Output Greater than the Kinetic Energy of an Imploding Shell at the National Ignition Facility, Phys. Rev. Lett. **120**, 245003 (2018).
[15] A. B. Zylstra, A. L. Kritcher, O. A. Hurricane, D. A. Callahan, K. Baker, T. Braun *et al.*, Record Energetics for an Inertial Fusion Implosion at NIF, Phys. Rev. Lett. **126**, 025001 (2021).
[16] D. Clery, Laser-powered fusion effort nears, "ignition", Science **373**, 841 (2021).
[17] J. Lindl, O. Landen, J. Edwards, and E. Moses, Review of the national ignition campaign 2009–2012, Phys. Plasmas **21**, 020501 (2014).
[18] National Nuclear Security Administration Report No. DOE/NA-0040.
[19] Lawrence Livermore National Laboratory Report No. LLNL-TR-810573.
[20] J. L. Kline *et al.*, Hohlraum energetics scaling to 520 TW on the National Ignition Facility, Phys. Plasmas **20**, 056314 (2013).
[21] R. Betti and O. A. Hurricane, Inertial-confinement fusion with lasers, Nat. Phys. **12**, 435 (2016).
[22] V. T. Tikhonchuk, T. Gong, N. Jourdain, O. Renner, F. P. Condamine, K. Q. Pan *et al.*, Studies of laser-plasma interaction physics with low-density targets for direct drive inertial confinement fusion on the Shenguang III prototype, Matter Radiat. Extremes **6**, 025902 (2021).
[23] V. N. Goncharov, S. Skupsky, T. R. Boehly, J. P. Knauer, P. McKenty, V. A. Smalyuk, R. P. J. Town, O. V. Gotchev, R. Betti, and D. D. Meyerhofer, A model of laser imprinting, Phys. Plasmas **7**, 2062 (2000).
[24] V. A. Smalyuk *et al.*, Review of hydrodynamic instability experiments in inertially confined fusion implosions on National Ignition Facility, Plasma Phys. Controlled Fusion **62**, 014007 (2020).
[25] X. Qiao and K. Lan, Novel Target Designs to Mitigate Hydrodynamic Instabilities Growth in Inertial Confinement Fusion, Phys. Rev. Lett. **126**, 185001 (2021).
[26] J. T. Hunt and D. R. Speck, Present and future performance of the Nova laser system, Opt. Eng. **28**, 461 (1989).
[27] T. Chang *et al.*, Laser hohlraum coupling efficiency on the Shenguang II facility, Phys. Plasmas **9**, 4744 (2002).
[28] M. Vandenboomgaerde, J. Bastian, A. Casner, D. Galmiche, J. P. Jadaud, S. Laffite, S. Liberatore, G. Malinie, and F. Philippe, Prolate-Spheroid (Rugby-Shaped) Hohlraum for Inertial Confinement Fusion, Phys. Rev. Lett. **99**, 065004 (2007).
[29] F. Philippe, A. Casner, T. Caillaud, O. Landoas, M. C. Monteil, S. Liberatore *et al.*, Experimental Demonstration of X-Ray Drive Enhancement with Rugby-Shaped Hohlraums, Phys. Rev. Lett. **104**, 035004 (2010).
[30] K. Lan, D. Lai, Y. Zhao, and X. Li, Initial study and design on ignition ellipraum, Laser Part. Beams **30**, 175 (2012).
[31] W. Y. Huo, K. Lan, Y. Li, D. Yang, S. Li, X. Li *et al.*, Determination of the Hohlraum *M*-Band Fraction by a Shock-Wave Technique on the SGIII-Prototype Laser Facility, Phys. Rev. Lett. **109**, 145004 (2012).
[32] T. Gong *et al.*, Recent research progress of laser plasma interations in Shenguang laser facilities, Matter Radiat. Extremes **4**, 055202 (2019).
[33] J. L. Miquel and E. Prene, LMJ & PETAL status and program overview, Nucl. Fusion **59**, 032005 (2019).
[34] Y. Ping *et al.*, Enhanced energy coupling for indirectly driven inertial confinement fusion, Nat. Phys. **15**, 138 (2019).
[35] D. W. Phillion and S. M. Pollaine, Dynamical compensation of irradiation nonuniformities in a spherical hohlraum illuminated with tetrahedral symmetry by laser beams, Phys. Plasmas **1**, 2963 (1994).
[36] S. A. Bel'kov *et al.*, Compression and heating of indirectly driven spherical fusion targets on the ISKRA-5 facility, Laser Part. Beams **17**, 591 (1999).
[37] J. M. Wallace, T. J. Murphy, N. D. Delamater, K. A. Klare, J. A. Oertel, G. R. Magelssen *et al.*, Inertial Confinement Fusion with Tetrahedral Hohlraums at OMEGA, Phys. Rev. Lett. **82**, 3807 (1999).
[38] K. Lan, X.-T. He, J. Liu, W. Zheng, and D. Lai, Octahedral spherical hohlraum and its laser arrangement for inertial fusion, Phys. Plasmas **21**, 052704 (2014).
[39] K. Lan, J. Liu, D. Lai, W. Zheng, and X.-T. He, High flux symmetry of the spherical hohlraum with octahedral 6LEHs at a golden hohlraum to-capsule radius ratio, Phys. Plasmas **21**, 010704 (2014).
[40] K. Lan and W. Zheng, Novel spherical hohlraum with cylindrical laser entrance holes and shields, Phys. Plasmas **21**, 090704 (2014).
[41] L. Ren, D. Zhao, and J. Zhu, Beam guiding system geometric arrangement in the target area of high-power laser drivers, High Power Laser Sci. Eng. **3**, e12 (2015).
[42] P. E. Masson-Laborde *et al.*, Laser plasma interaction on rugby hohlraum on the Omega Laser Facility: Comparisons

between cylinder, rugby and elliptical hohlraums, Phys. Plasmas **23**, 022703 (2016).
[43] W. A. Farmer, M. Tabak, J. H. Hammer, P. A. Amendt, and D. E. Hinkel, High-temperature hohlraum designs with multiple laser-entrance holes, Phys. Plasmas **26**, 032701 (2019).
[44] W. Y. Wang and R. S. Craxtona, Pentagonal prism spherical hohlraums for OMEGA, Phys. Plasmas **28**, 062703 (2021).
[45] X. T. He, J. W. Li, Z. F. Fan, L. F. Wang, J. Liu, K. Lan, J. F. Wu, and W. H. Ye, A hybrid-drive nonisobaric-ignition scheme for inertial confinement fusion, Phys. Plasmas **23**, 082706 (2016).
[46] E. M. Campbell, V. N. Goncharov, T. C. Sangster, S. P. Regan, P. B. Radha, R. Betti *et al.*, Laser-direct-drive program: Promise, challenge, and path forward, Matter Radiat. Extremes **2**, 37 (2017).
[47] K. Lan, J. Liu, Z. Li, X. Xie, W. Huo, Y. Chen *et al.*, Progress in octahedral spherical hohlraum study, Matter Radiat. Extremes **1**, 8 (2016).
[48] W. Y. Huo, Z. Li, D. Yang, K. Lan, J. Liu, G. Ren *et al.*, First demonstration of improving laser propagation inside the spherical hohlraums by using the cylindrical laser entrance hole, Matter Radiat. Extremes **1**, 2 (2016).
[49] W. Y. Huo, Z. Li, Y. H. Chen, X. Xie, K. Lan, J. Liu *et al.*, First Investigation on the Radiation Field of the Spherical Hohlraum, Phys. Rev. Lett. **117**, 025002 (2016).
[50] K. Lan, Z. Li, X. Xie, Y. H. Chen, C. Zheng, C. Zhai *et al.*, Experimental demonstration of low laser-plasma instabilities in gas-filled spherical hohlraums at laser injection angle designed for ignition target, Phys. Rev. E **95**, 031202(R) (2017).
[51] Y. Chen, Z. Li, X. Xie, C. Zheng, C. Zhai, L. Hao *et al.*, First experimental comparisons of laser-plasma interactions between spherical and cylindrical hohlraums at SGIII laser facility, Matter Radiat. Extremes **2**, 77 (2017).
[52] W. Y. Huo, Z. Li, Y. H. Chen, X. Xie, G. Ren, H. Cao *et al.*, First Octahedral Spherical Hohlraum Energetics Experiment at the SG-III Laser Facility, Phys. Rev. Lett. **120**, 165001 (2018).
[53] H. Zhao *et al.*, Progress in optical Thomson scattering diagnostics for ICF gas-filled hohlraums, Matter Radiat. Extremes **4**, 055201 (2019).
[54] K. Lan, T. Feng, D. Lai, Y. Xu, and X. Meng, Study on two-dimensional transfer of radiative heating wave, Laser Part. Beams **23**, 275 (2005).
[55] H. Yong, P. Song, C.-L. Zhai, D.-G. Kang, J.-F. Gu, X.-D. Hang, P.-J. Gu, and S. Jiang, Numerical simulation of 2-D radiation-drive ignition implosion process, Commun. Theor. Phys. **59**, 737 (2013).
[56] H. Cao, Y.-H. Chen, C. Zhai, C. Zheng, and K. Lan, Design of octahedral spherical hohlraum for CH Rev5 ignition capsule, Phys. Plasmas **24**, 082701 (2017).
[57] G. Ren, K. Lan, Y.-H. Chen, Y. Li, C. Zhai, and J. Liu, Octahedral spherical hohlraum for Rev. 6 NIF beryllium capsule, Phys. Plasmas **25**, 102701 (2018).
[58] D. Yuan, J. Wu, Y. Li, X. Lu, J. Zhong, C. Yin *et al.*, Modeling supersonic-jet deflection in the Herbig-Haro 110-270 system with high-power lasers, Astrophys. J. **815**, 46 (2015).
[59] J. Gu, Z. Dai, P. Song, S. Zou, W. Ye, W. Zheng, P. Gu, J. Wang, and S. Zhu, Asymmetric-shell ignition capsule design to tune the low-mode asymmetry during the peak drive, Phys. Plasmas **23**, 082703 (2016).
[60] L. Hao, Y. Zhao, D. Yang, Z. Liu, X. Hu, C. Zheng *et al.*, Analysis of stimulated Raman backscatter and stimulated Brillouin backscatter in experiments performed on SG-III prototype facility with a spectral analysis code, Phys. Plasmas **21**, 072705 (2014).
[61] [H. Liu, H. Song, Q. Zhang, G. Zhang, and Y. Zhao, Validation for equation of state in wide regime: Copper as prototype, Matter Radiat. Extremes **1**, 123 (2016).
[62] F. J. D. Serduke, E. Minguez, S. J. Davidson, and C. A. Iglesias, WorkOp-IV summary: Lessons from iron opacities, J. Quant. Spectrosc. Radiat. Transfer **65**, 527 (2000).
[63] K. Lan, X. Qiao, P. Song, W. Zheng, B. Qing, and J. Zhang, Study on laser-irradiated Au plasmas by detailed configuration accounting atomic physics, Phys. Plasmas **24**, 102706 (2017).
[64] R. S. Cohen, L. Spitzer, and P. M. Routly, The electrical conductivity of an ionized gas, Phys. Rev. **80**, 230 (1950).
[65] L. Spitzer and R. Härm, Transport phenomena in a completely ionized gas, Phys. Rev. **89**, 977 (1953).
[66] Y. Zhao, K. Lan, P. Song, W. Zheng, and X. Li, A method to determine the flux limiter via the motion of the *M*-band emission region in Au hohlraum, Laser Part. Beams **30**, 387 (2012).
[67] A. L. Kritcher *et al.*, Metrics for long wavelength asymmetries in confinement fusion implosion on the National Ignition Facility, Phys. Plasmas **21**, 042708 (2014).
[68] K. Ren *et al.*, Direct measurement of x-ray flux for a prespecified highly-resolved region in hohlraum, Opt. Express **23**, A1072 (2015).
[69] Q. Wang, B. Deng, Z. Cao, T. Chen, and K. Deng, Development of a gated x-ray imager with multiple views and spectral selectivity for observing plasmas evolution in hohlraums, Rev. Sci. Instrum. **90**, 073301 (2019).
[70] Z. C. Li *et al.*, A novel flat-response x-ray detector in the photon energy range of 0.1–4 keV, Rev. Sci. Instrum. **81**, 073504 (2010).
[71] L. Guo *et al.*, A compact flat-response x-ray detector for the radiation flux in the range from 1.6 keV to 4.4 keV, Meas. Sci. Technol. **23**, 065902 (2012).
[72] See Supplemental Material at http://link.aps.org/supplemental/10.1103/PhysRevLett.127.245001 for optimum repointing scheme on the SGIII, simulation codes, diagnostics, implosion diagram and hydrodynamic instabilities, laser backscatter analysis, asymmetry calculation, and asymmetries for shot SGIII20190102003.
[73] H.-S. Park, O. A. Hurricane, D. A. Callahan, D. T. Casey, E. L. Dewald, T. R. Dittrich *et al.*, High-Adiabat High-Foot Inertial Confinement Fusion Implosion Experiments on the National Ignition Facility, Phys. Rev. Lett. **112**, 055001 (2014).

Correction: The parenthetical phrases in the caption to Fig. 3 contained errors and have been set right.